Geochemistry Geophysics Geosystems G3
AN ELECTRONIC JOURNAL OF THE EARTH SCIENCES
Published by AGU and the Geochemical Society

Article
Volume 4, Number 9
18 September 2003
1079, doi:10.1029/2003GC000511
ISSN: 1525-2027

Geodynamic implications of xenolith geotherms

Norman H. Sleep
Department of Geophysics, Stanford University, Stanford, California 94305, USA (norm@geo.stanford.edu)

[1] Studies of xenolith suites yield depth-temperature arrays for the lithosphere at the time of eruption. These studies constrain the conductive heat flow through the lithosphere and limit the temperature range across the rheological boundary layer to <300 K. Numerical models of convection illustrate features that may be found within suites of samples. An individual dike may sample the geotherm along a finite length of its strike having variable geotherms, causing scatter in the depth-temperature array. In a suite from the Slave Province of Canada, local heating within a deep stockwork is a more likely cause of scatter. Plume material ponded beneath a craton may yield a linear array extrapolating to the shallow geotherm without any noticeable kink or curvature. This situation existed beneath Lesotho in South Africa at ~90 Ma. Convection at the base of the lithosphere may produce stress concentrations that trigger dike formation. Dikes may stagnate and form stockworks in low-stress regions above the thermal boundary layer.

Components: 9900 words, 15 figures.

Keywords: Mantle plumes; kimberlite; geotherm; hot spot; convection; craton.

Index Terms: 8120 Tectonophysics: Dynamics of lithosphere and mantle—general; 8110 Tectonophysics: Continental tectonics—general (0905); 8121 Tectonophysics: Dynamics, convention currents and mantle plumes.

Received 15 January 2003; **Revised** 16 July 2003; **Accepted** 7 August 2003; **Published** 18 September 2003.

Sleep, N. H., Geodynamic implications of xenolith geotherms, *Geochem. Geophys. Geosyst.*, *4*(9), 1079, doi:10.1029/2003GC000511, 2003.

1. Introduction

[2] Kimberlites (*sensu latu*) carry xenoliths from great depths in the mantle to the surface. Petrologists determine the temperature and pressure of each xenolith and hence xenolith geotherms [e.g., *Rudnick and Nyblade*, 1999]. A key result is that the xenolith geotherm intersects the MORB adiabat at similar depths beneath the large cratons, ~200 km.

[3] The purpose of this paper is to apply heat and mass transfer principles to examine what can be learned from xenolith temperature-pressure arrays. The basic issue is straightforward. The xenoliths from a single kimberlite provide an instantaneous snapshot of the mantle beneath the site as ascent takes hours to days [e.g., *Anderson*, 1979; *Spera*, 1984; *Kelley and Wartho*, 2000]. Rapid ascent is necessary to preserve diamonds and to keep xenoliths entrained. However, the samples in a single eruption may come laterally from a finite along-strike distance of the kimberlite dike. A suite of kimberlites samples the geotherm at various times and places. Some of these may predate, be concurrent with, or postdate plume activity [e.g., *Bell et al.*, 2003]. Random sampling of the lithosphere by kimberlites, as well as any systematic bias in the location of kimberlites may cause similar cratons to look different and obscure real differences between cratons.

[4] I address a variety of topics where the principles of heat and mass transfer shed some light on xenoliths. The intent is to aid petrologists who analyze and interpret xenolith data. The topics relate to the variation of temperature on the length scale (tens of km) of the rheologically active thermal boundary layer, rather than craton-wide variations. I compute evolution of the temperature field after plume material ponds beneath the craton in section 2 and well as the ambient temperature field in the absence of plume. This yields an array of possible geotherms for likely geological situations. My objective is to obtain the local variation in the geotherm beneath various places as well as systematic effects of plume material on the geotherm. I discuss xenolith suites from the Slave Craton in Canada and Lesotho in Southern Africa in section 3 with emphasis on the topics of local variation of the geotherm sampled along a dike, local perturbation of the temperature by metasomatism, and the geotherm above ponded plume material. I discuss stress within the lithosphere with respect to what can be learned from sheared and coarse xenoliths in section 4.

2. Heat and Mass Transfer Theory

[5] The objective of this section is to obtain temperature field near the base of cratonic lithosphere for comparison with temperature-depth estimates from xenoliths in section 3. To do this, I numerically solve the heat and mass transfer equations. The mathematics and the physical parameters are discussed in section 2.1 and the numerical results present in section 2.2. I use scaling techniques, collectively called parameterized convection to explain and generalize the results. The numerical model follows that of *Andrews* [1972]. *Sleep* [2002, 2003] discusses it in detail. The stress and strain fields associated with convection are obtained as a byproduct for use in section 4.

2.1. Physical and Mathematical Model

[6] I solve the combined heat flow and force balance equations to obtain the temperature field beneath cratons. I do this numerically in 2 dimensions. The heat flow equation is

$$\frac{\partial T}{\partial T} + \mathbf{V} \cdot \nabla T = \kappa \nabla^2 T, \tag{1}$$

where T is potential temperature, t is time, $\mathbf{V}$ is velocity, and κ is thermal diffusivity. For simplicity, there are no heat sources. Crustal radioactivity is too shallow to affect the dep processes at the base of the lithosphere and the heat generation in the mantle is likely to be small. The vertical component of the momentum equation in three-dimensions is

$$\frac{\partial \tau_{xz}}{\partial x} + \frac{\partial \tau_{yz}}{\partial y} + \frac{\partial \tau_{zz}}{\partial z} - \frac{\partial P}{\partial z} + \Delta \rho g = 0, \tag{2}$$

where x is the horizontal coordinate in the plane of the convection cell and y is horizontal coordinate perpendicular to that plane in the direction of plate motions, z is depth, and P is the "scalar" pressure, τ_{ij} is the deviatoric stress tensor, $\Delta\rho = -\alpha\rho\Delta T$ is the excess density from temperature, α is the volume thermal expansion coefficient, ρ is a reference density, and ΔT is the temperature above the mantle adiabat.

[7] Certain physical parameters in equations (1)–(2) are reasonably well constrained. I assume that these parameters are constant in my calculations. These include the thermal conductivity $k = 3$ W m^{-1} K^{-1}, the specific heat per volume is $\rho C = 4$ MJ m^{-3} K^{-1}, the thermal diffusivity is, the density is 3400 kg m^{-3}; and the thermal expansion coefficient is $\alpha = 3 \times 10^{-5}$ K^{-1}. The acceleration of gravity is constant at $g = 9.8$ m^2 s^{-1}. The mantle MORB adiabat extrapolates to 1300°C at the surface.

[8] I keep the rheology simple and let the linear viscosity be a function of temperature

$$\eta = \eta_0 \exp\left[\frac{-\Delta T}{T_\eta}\right], \tag{3}$$

where η_0 is the viscosity at the mantle adiabat, ΔT is the temperature above the mantle adiabat, and T_η is the temperature scale for viscosity. I use T_η = 60 K in all the calculations. I ignore the effects of chemically different cratonal lithosphere on density and viscosity [e.g., *Doin et al.*, 1997] for brevity. The models in this paper serve to illustrate

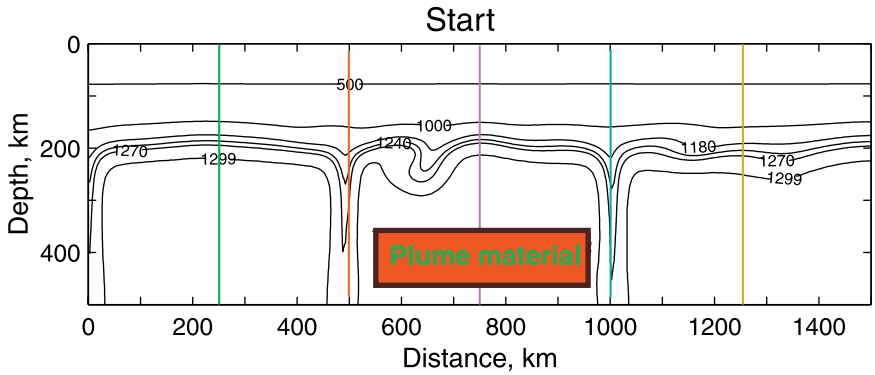

Figure 1. The computed potential temperature field just before I impose plume material (red rectangle) on the domain of the calculation. Vigorous local downwellings exist between broad upwellings. The contour intervals are 500, 1000, 1100, 1180, 1240, 1270, and 1299°C. The mantle adiabat is 1300°C and the plume material is 1600°C. Vertical lines indicate positions of geotherms shown in Figure 2.

probable effects without introducing this important but complicated topic. *O'Neill et al.* [2003] discuss the effect of a chemical root stabilizing cratons and the effect of the finite extent of the craton on its thermal structure in the convecting mantle.

[9] Equations (1)–(3) result in a formal initial value and boundary value problem. I impose a 1500-km wide region so that the artificial side boundaries (free slip and no heat flow) are well out of the way of the central region of interest. I impose a permeable bottom boundary that lets cold fluid exit the domain and warm fluid to enter at the MORB adiabat [*Moore et al.*, 1999]. The upper boundary condition represents the rigid isothermal (0°C) surface of the craton.

[10] The initial condition represents that the craton has existed for over 2 b.y. and that convective heat flow at the base is essentially in equilibrium with conduction through the crust. I begin with a conductive linear thermal gradient from the surface down to 200-km depth. The conductive heat flow is then 19.5 mW m^{-3}. I set the viscosity at the MORB (mid-oceanic ridge basalt) adiabat to 0.657×10^{19} Pa s so that the initial state is near the equilibrium state. That is, the initial conductive heat flow is the predicted convective heat flow,

$$q_v = 0.47 k T_\eta^{4/3} \left[\frac{\rho g \alpha}{\kappa \eta_H}\right]^{1/3}, \quad (4)$$

where η_H is the viscosity of the adiabatic halfspace (here η_0) [*Davaille and Jaupart*, 1993a, 1993b, 1994]. I slightly perturb the initial temperature and let convection proceed for 90 m.y. so that a representative temperature field is reached.

2.2. Numerical Model Without Plume Material

[11] Figure 1 shows the convection pattern beneath a normal craton. It illustrates the well-known unsteady nature of stagnant-lid convection [*Solomatov*, 1995; *Solomatov and Moresi*, 2000]. Vigorous internal downwellings occur at ~500 km and ~1000 km. A downwelling is starting at ~650 km. Broad upwellings balance this flow.

[12] Figure 2 shows geotherms selected at 250-km spacings. The geotherms at 500 km and 1000 km are within downwellings. The geotherm at 1250 km is within a nascent downwelling. The geotherm at 250 km is near the center of an upwelling and the geotherm at 750 km is within a local upwelling near an incipient downwelling. The geotherms within upwellings are slightly hotter than the lateral average.

[13] The curved segment at the base of the geotherm is associated with the rheologically active boundary layer. *Solomatov* [1995] and *Solomatov and Moresi* [2000] show that temperature range across the rheologically active boundary layer is

$$\Delta T_{\text{rheo}} = 1.2(n+1) = 2.4 T_\eta. \quad (5)$$

where n is the exponent of the power law rheology and the second equality is the linear (Newtonian)

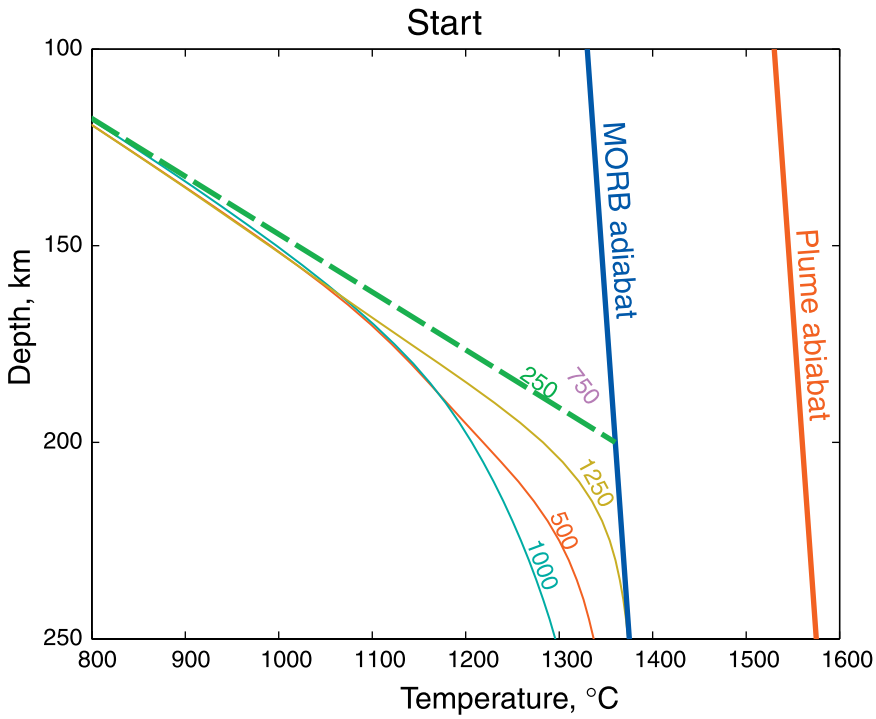

Figure 2. Computed geotherms at 250-km intervals from Figure 1. The MORB adiabat and the plume adiabat have gradients of 0.3 K km^{-1}. They intersect the surface at 1300°C and 1500°C, respectively. The dashed green line is the expected laterally averaged conductive geotherm.

n = 1 result. For T_η = 60 K, this range is 144 K. The curved segment of the geotherms is somewhat narrower within the upwellings and wider in the downwellings.

[14] This situation results because the upwellings are broad, while the downwellings are narrow. Conduction depresses the isotherms in the nearly rigid lithosphere above narrow downwellings. Quantitatively, the convective heat flow scales with the conductive heat flow through the rigid lid

$$q = k\frac{T_L}{Z_L}, \tag{6}$$

where T_L is the temperature contrast across the lithosphere and Z_L is the thickness of the lithosphere. The convective heat flow within the broad upwellings is dimensionally

$$q = \rho C V_U T_\eta, \tag{7}$$

where V_U is the upward velocity. Solving (6) and (7) yields

$$V_U = \frac{\kappa T_L}{Z_L T_\eta}. \tag{8}$$

I recover the scale length for conduction dominating over convection,

$$Z_U \equiv \frac{\kappa}{V_U} = \frac{Z_L T_\eta}{T_L}, \tag{9}$$

which is obtained more simply by noting that conduction and convection are comparable in the boundary layers.

[15] Equations (7) through (9) apply dimensionally to the narrow downwellings. However, the ratio of the upward to the downward velocity scales with the relative area occupied by upwellings and narrow downwellings

$$V_D = V_U\frac{A_U}{A_D}, \tag{10}$$

where V_U is the upward velocity within the rheologically active boundary layer, V_D is the velocity within the narrow downwellings, A_D is the area occupied by narrow downwellings, and A_U is the area occupied by upwellings within the rheologically active boundary layer. From Figure 1,

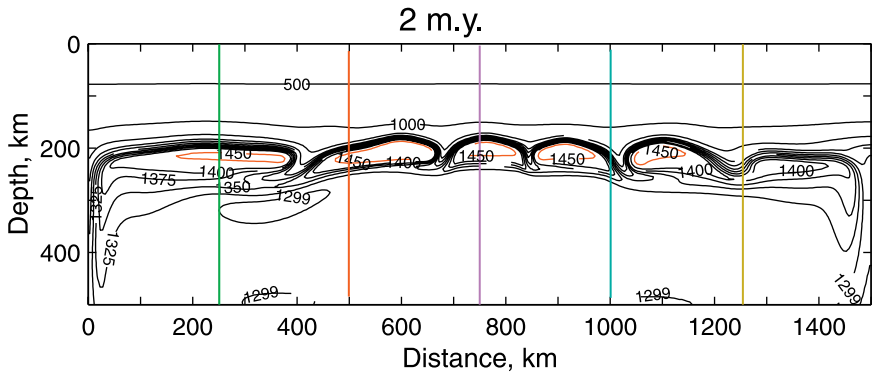

Figure 3. The computed potential temperature field at 2 m.y after I imposed plume material as in Figure 1. Vigorous local downwellings exist within the ponded plume material. The contour intervals are 500, 1000, 1100, 1180, 1240, 1270, 1299, 1325, 1350, 1375, 1400, and 1450°C. I show the 1450°C contour is shown in red to delineate the hottest plume material. The downwellings of hot material on the sides are an artifact of the artificial boundary condition. The return flow from upwelling plume material stirred the sides of the domain of calculation. Vertical lines indicate positions of geotherms shown in Figure 4.

the area ratio is ~10 and the downwelling velocity is ~10 times that in equation (8).

[16] The downwellings stir the fluid in the isoviscous region beneath the boundary layer. The upwelling velocity below the rheological boundary layer is thus much greater than the velocity within the layer. The scale length in equation (9) is proportionally reduced. The downward tails of the geotherms thus approach the adiabat more rapidly than they would if the vertical velocity remained constant with depth.

2.3. Numerical Models With Plume Material

[17] I inserted plume material into the domain of the calculation just after the time in Figure 1. The initial geometry and temperature are unrealistic but do yield realistic conditions once the plume has ponded beneath the lithosphere. I impose plume material with a potential temperature 1600°C within a rectangular region between 350 and 450 km depth and 550 to 950 km laterally. I intend this as a simple way of representing a starting plume head in two dimensions. The plume material ascends to the surface and ponds at the base of the lithosphere. In doing this, it entrains normal mantle and becomes a broader but less hot region. The initial hot region is equivalent to a 40-km thick region with an excess temperature of 200 K ponded over the domain of the model. This is about the final thickness to which a starting plume head spreads beneath a flat surface [*Sleep et al.*, 2003]. The fate of the plume material once ponded, rather than the details of its ascent that cannot be studied in two dimensions, is the objective of the calculations.

[18] Figure 3 shows the potential temperature 2 m.y. after the insertion of the plume material. The plume material ponds at the base of the lithosphere. The pre-plume relief at the base of the lithosphere acts as catchments and modulates convection. The stable boundary at the base of the plume material confines downwelling.

[19] The geotherms at 1000 and 1250 km are within downwellings (Figure 4). The geotherm at 500 km is at the edge of a downwelling. Hot plume material exists beneath a somewhat cooler than average geotherm. The 250-km and 750-km geotherms are within catchments of ponded plume material. These geotherms are nearly linear until they reach their maximum temperature.

[20] At later times, much of the plume material has cooled below the mantle adiabat. The illustrations show the region that is still hotter than the mantle adiabat, that is the "hot" plume material. Figure 5

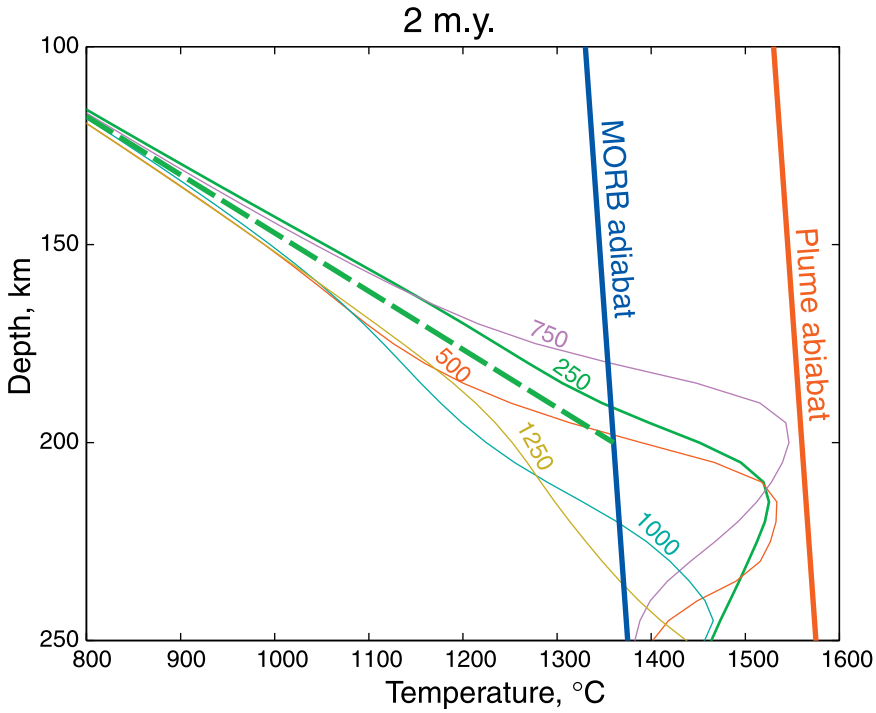

Figure 4. Computed geotherms at 250-km intervals 2 m.y. after the imposition of plume material as in Figure 2.

shows the situation after 10 m.y. The maximum temperature of the plume material has decreased by ~100 K from that in Figure 3. The downwellings are starting to penetrate the base of the hot plume material. The geotherms at 250 km and 750 are elevated above the initial geotherm (Figure 6). The geotherm at 1250 km is similar to the initial average but is underlain by warm plume material. The rapid lateral variability occurs along the edges of the downwellings. Figure 7 illustrates closely spaced geotherms as might be sampled along strike over 25 km by a dike.

[21] Little hot plume material remains after 20 m.y. (Figure 8). The previous catchments modulate the convection into closely spaced upwellings. The geotherms at 250 and 750 km are well elevated above their initial values (Figure 9).

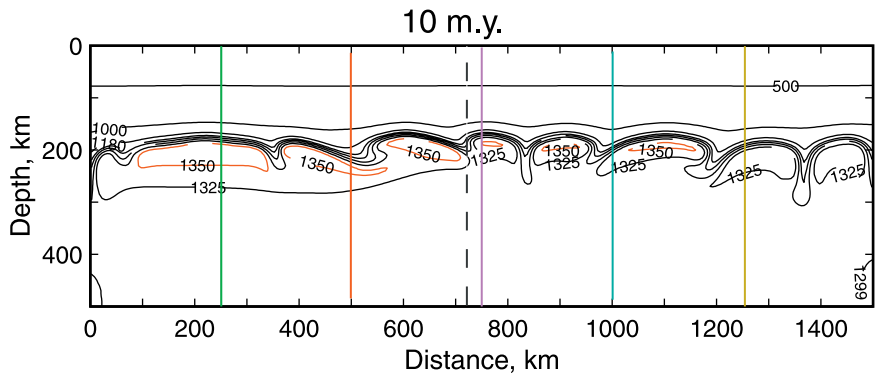

Figure 5. The computed potential temperature field at 10 m.y as in Figure 1. Vigorous local downwellings penetrate through the ponded plume material. The contour intervals are 500, 1000, 1100, 1180, 1240, 1270, 1299, 1325, and 1350°C. I show the 1350°C contour in red to delineate the hottest remaining plume material. Solid vertical lines indicate positions of geotherms shown in Figure 6. The dashed vertical line indicates the closely spaced geotherms in Figure 7.

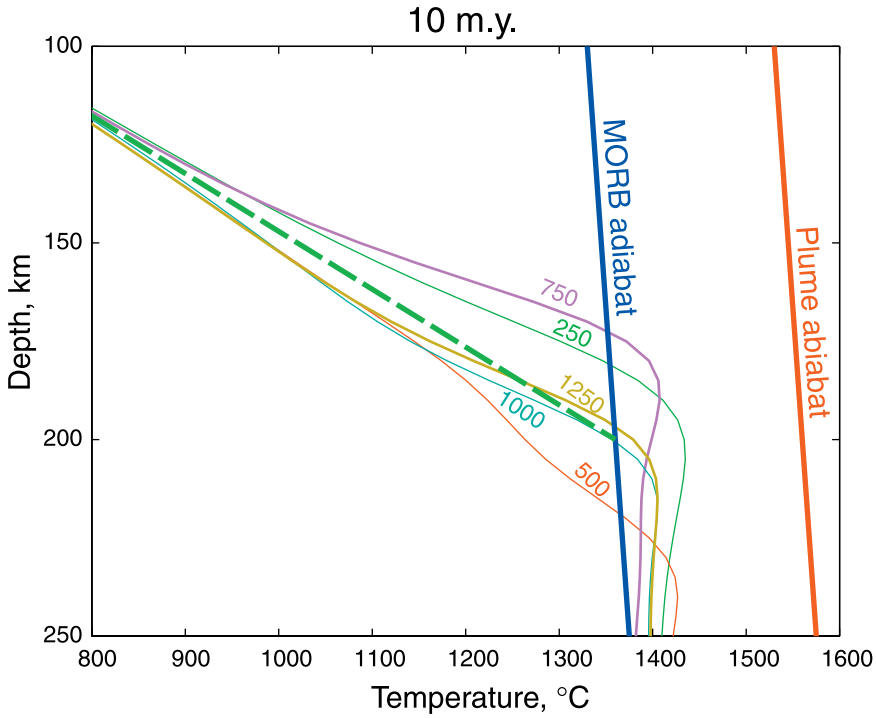

Figure 6. Computed geotherms at 250-km intervals from the temperature field at 10 m.y. as in Figure 2.

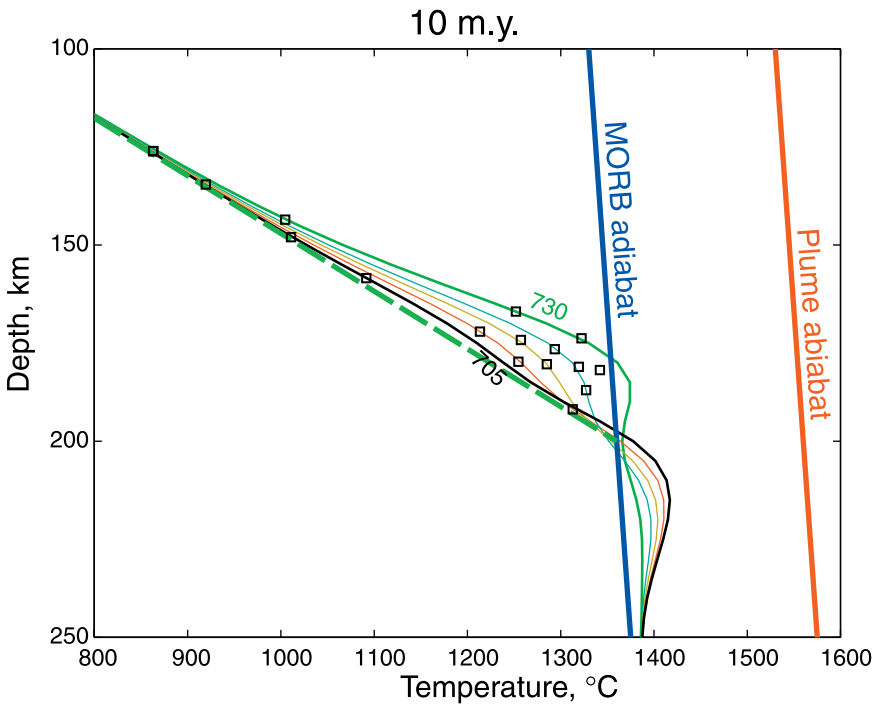

Figure 7. Computed geotherms at 10 m.y. at 5-km intervals as might be sampled along strike by a dike. The points illustrate the scatter that might occur in an array of xenoliths.

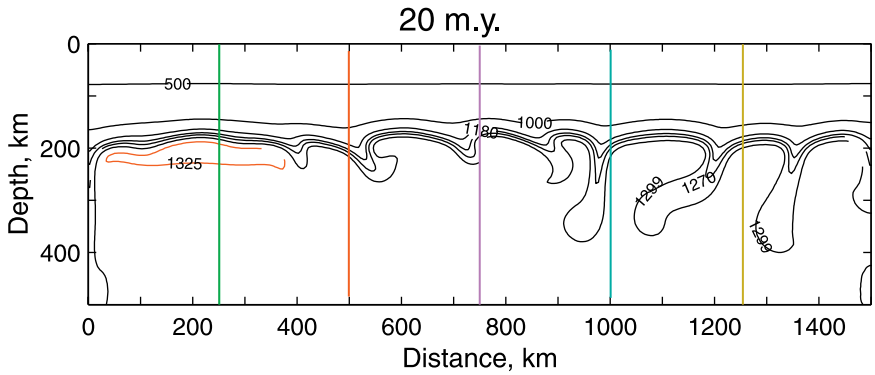

Figure 8. The computed potential temperature field at 20 m.y as in Figure 1. Vigorous local downwellings exist and most of the region is cooler than the mantle adiabat. The contour intervals are 500, 1000, 1100, 1180, 1240, 1270, 1299, and 1325°C. I show 1325°C contour in red to delineate the hottest plume material. Vertical lines indicate positions of geotherms shown in Figure 9.

[22] By 60 m.y., the temperature field (Figure 10) resembles that at the start in Figure 1. The differences are subtle. For example, the geotherms that were most affected by the plume at 250 and 750 km in Figure 11 remain elevated from those in Figure 2.

3. Comparison With Xenolith Data

[23] The models in section 2 illustrate the normal temperature field beneath cratons and the temperature field following a plume event. Yet, the connection of kimberlites to plumes is not obvious. It is obvious that hot ponded plume material and the overlying lithospheric material heated by it have a greater fraction of partial melt than material of the same compositions at the MORB adiabat. The ponded plume material aids the escape of melt by putting the lithosphere in horizontal tension, It is also not clear whether temperature or favorable stress concentrations are the more limiting factor in

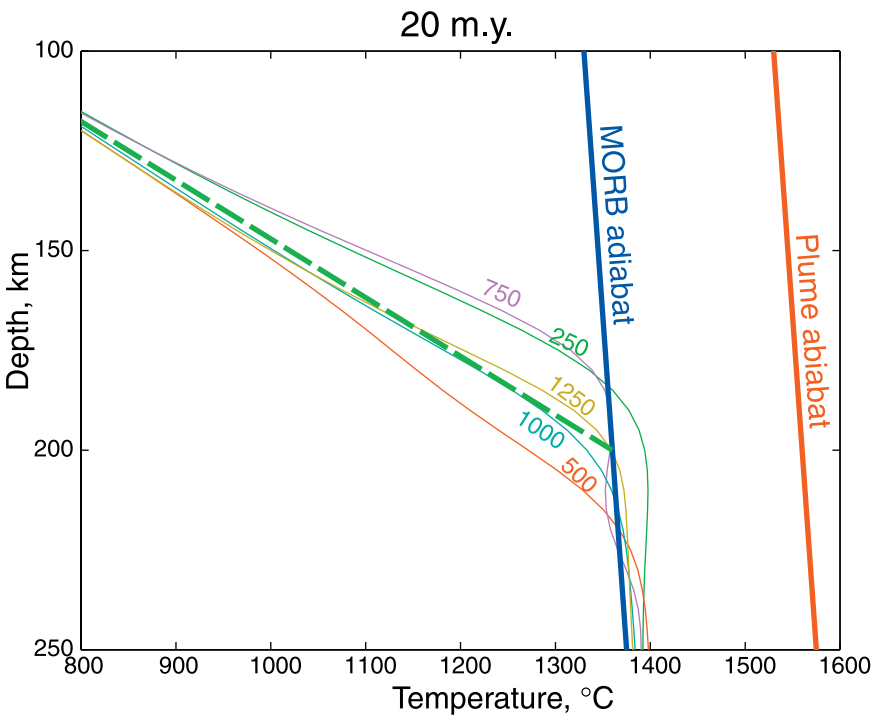

Figure 9. Computed geotherms at 20 m.y. at 250-km intervals as in Figure 2.

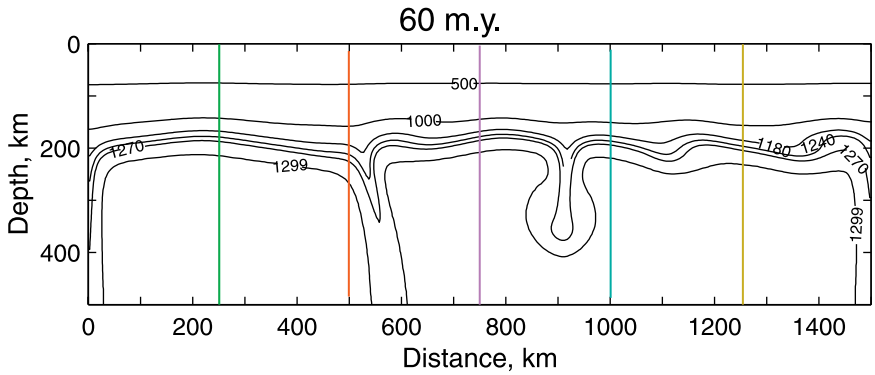

Figure 10. The computed potential temperature field at 60 m.y as in Figure 1. The region is cooler than the mantle adiabat. The contour intervals are 500, 1000, 1100, 1180, 1240, 1270, and 1299°C. The situation is similar to that in the starting model in Figure 1. Vertical lines indicate positions of geotherms shown in Figure 11.

kimberlite eruption. In the former case, kimberlites preferentially nucleate at the top of upwellings and from the hottest and highest ponded plume material. In the latter case, they may nucleate at the edges of downwellings where strain rates and stresses are the highest. I am unable to resolve this issue with available data.

[24] I select xenolith data from the Slave province in Canada and Lesotho in Southern Africa. The Slave data are from a single eruption and illustrate the implication of the calculations to that situation. The Lesotho data are from several kimberlites spread out over a broad region and illustrate the effects of ponded plume material.

[25] For the most part, I take the xenolith pressures and temperatures at face value. I realize that neither the relative nor the average temperatures and pressures are perfect [e.g., *Bell et al.*,

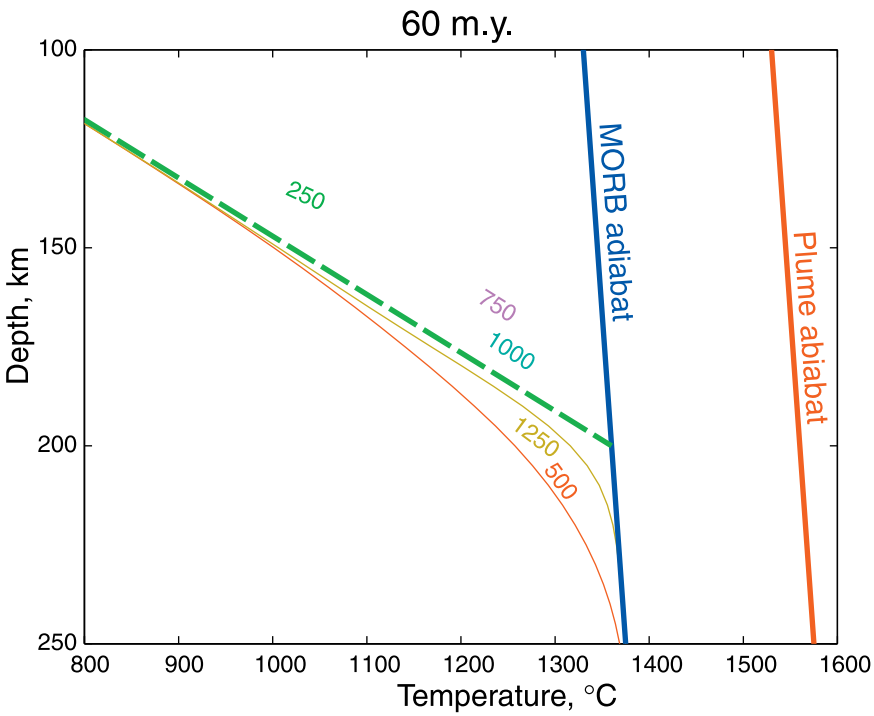

Figure 11. Computed geotherms at 60 m.y. at 250-km intervals as in Figure 2. The 250 and 750-km geotherms are somewhat hotter than the where before were before the plume material ponded in Figure 2.

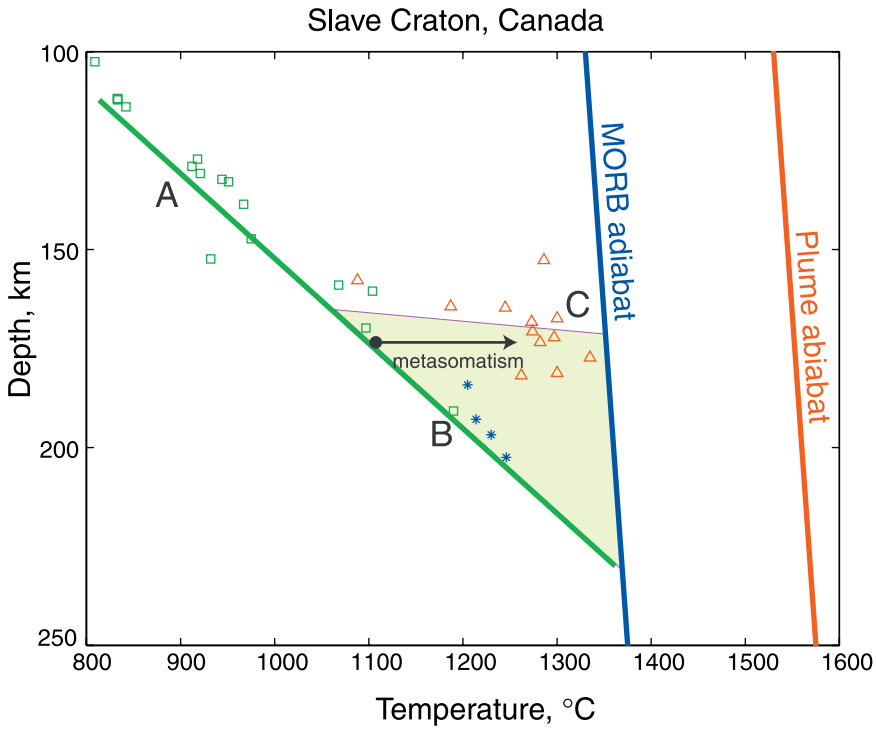

Figure 12. Observed depth and temperature for xenoliths from the Jericho pipe Canada. Data after *Kopylova et al.* [1999b], using the *Brey and Köhler* [1990] method. (Depth as function of pressure is $(P - \rho_C g Z_C)/(\rho g) + Z_C$, where the crustal density ρ_C is 3000 kg m^{-3}, the crustal thickness (Z_C) is 35 km, and the mantle density is ρ is 3400 kg m^{-3}.) Green squares represent coarse xenoliths; red triangles represent sheared xenoliths, and blue asterixes represent megacrystalline xenoliths. The green line is the inferred regional geotherm determined by the shallow point group A. The geotherm extrapolates into the deep point group B. Point group C is hotter than this geotherm. Heating proportional to the area of the green triangle (eyeball fit) is needed to raise the regional temperature to the trend indicated by point group C. The effects of metasomatism would locally raise the temperatures of xenoliths without changing the depth.

2003]. The methods for determining the xenolith geotherm and the MORB and plume adiabats are different and thus may not be completely consistent. For the most part, these data are internally consistent. It is valuable to put my discussion in the context of real data. I address the issue of stresses and sheared xenoliths in section 4.

3.1. Jericho Pipe, Slave Province in Canada

[26] The Jericho Pipe in the Slave Province represents a single complex eruptive event at 172 Ma [*Cockenboo*, 1999; *Heaman and Kjargaard*, 2002]. It is part of a dike complex with a strike length of ~14 km. The coarse xenoliths define a linear geotherm with minor scatter (Figure 12, points group A) [*Kopylova et al.*, 1999a, 1999b]. As occurs in general, any real curvature in the trend associated with variation in the conductivity with depth or variation of heat flow with depth from radioactive heat generation cannot be resolved. Following *Rudnick and Nyblade* [1999], I do not attempt to resolve these effects.

[27] There is much scatter in the P-T array beneath ~160 km [*Kopylova et al.*, 1999a, 1999b]. There is a single coarse xenolith point at ~1200°C and ~200 km and four nearby points for megacrystalline pyroxenite (point group B). These 5 points are not on the same geotherm as the sheared "porphyroclastic" xenoliths (point group C). It is conceivable that the coarse xenoliths re-equilibrated more slowly than sheared ones and reflect the temperature field before the region below 160-km depth heated up. The megacrystalline pyroxenites are a locally abundant intrusive rock [*Kopylova et al.*, 1999b].

[28] Salient features in the pressure-temperature array include the coarse xenolith outlier, the pyroxenites, and the scatter in the sheared xenolith points. They features serve to introduce the concepts the lateral variability of xenoliths sampled by a single pipe, the aftermath of plumes, and the effects of metasomatism on the P-T array.

3.1.1. Plume-Related Effects

[29] It is tempting to associate features of the xenolith P-T array in Figure 12 with plumes. In any case, the data serve to illustrate the expected geotherm in the aftermath of a plume. The geotherm defined by the shallow, coarse, and deep, sheared xenoliths resembles the model geotherms computed for 10 m.y. (Figure 6) and 20 m.y. (Figure 9). That is, the ponded plume material has cooled and its heat has thinned the base of the lithosphere. The area of the light green triangle in Figure 12 is proportional to the heat per area in the ponded plume material,

$$\frac{1}{2} Z_X \Delta T_X = Z_P \Delta T_P \tag{11a}$$

where Z_X is the depth range of the triangle in Figure 12, ΔT_X is the temperature range of the triangle, Z_P is the thickness of the ponded plume material, and ΔT_P is the excess temperature of the ponded plume material. On Figure 12, the depth range is ~50 km and the temperature range is ~250 K. Letting the temperature excess of the plume material be 200 K yields its thickness of ~31 km. This is comparable to the 40 km assumed in the models.

[30] The temperature anomaly eventually reaches the surface, increasing the heat flow at all depths within the lithosphere and reducing thickness of the lithosphere by Z_X. Equation (11a) then becomes

$$\frac{1}{2} \Delta Z_L T_L = Z_P \Delta T_P \tag{11b}$$

where ΔZ_L is the change in lithospheric thickness. Letting T_L be 1300°C and assuming a 40-km thickness of plume material with an excess temperature of 200 K implies that the lithosphere thins by 12 km. *Bell et al.* [2003] infer similar lithospheric thinning from the differences between older and younger xenolith geotherms in Southern Africa.

[31] Given the complexity of the eruption sequence [*Cockenboo*, 1999], the observed along-strike distance of the Jericho-related dikes of ~14 km, and tens of km extent of some dikes in Lesotho [*Nixon*, 1973], along-strike mingling is a plausible explanation for the scatter in Figure 12. (As discussed in section 4, the deeper part of the dike may also have nonvertical dip.) The geotherms at the edge of an upwelling in Figure 7 lie between the original conductive geotherm and those for a lithosphere about ~25 km thinner. This is a factor of ~2 less than the observed scatter in Figure 12. It is, however, about the amplitude of the systematic trend away from the shallow convective geotherm. I conclude that a plume event 10–20 m.y. before the time of kimberlite eruption is an initially attractive explanation for the systematic trend. Some but not all of the scatter may owe to along-strike mingling of xenoliths by the dike.

[32] A significant problem with the plume heating hypothesis is that the Slave craton does not lie along a well-known plume track at ~192-Ma. The Monteregian-New England Seamount track is the most likely candidate [*Heaman and Kjargaard*, 2000]. The track obtained from kimberlite volcanism at 175 Ma was at the northwest end of James Bay. This region is 2000 km southeast. *Heaman and Kjargaard* [2000] continue their track to the northwest end of Hudson Bay at 197 Ma, ~1000 km from Jericho. The association of the Jericho pipes with plumes is tenuous enough that consideration of alternatives is warranted.

3.1.2. Metasomatic Effects

[33] *Kopylova et al.* [1999a, 1999b] note that the sheared xenoliths have been metasomatized. The heating by the metasomatizing fluid is a good explanation for observation that the sheared xenoliths were hotter than the extrapolated conductive geotherm and for the scatter in their P-T array.

[34] Heat and mass balance indicates that this metasomatism was a local feature in the mantle. The Jericho kimberlite formed by 0.7 to 0.9% melting of a CO_2-rich and H_2O-rich region of the

mantle [*Price et al.*, 2000]. The small volumes of kimberlites are more telling if one considers CO_2, which has an abundance of ~17% in the Jericho kimberlite [*Price et al.*, 2000] and ~72 ppm in average upper mantle [*Saal et al.*, 2002]. This implies that the kimberlite could compose only 0.04% of the average mantle. In general, kimberlitic magmas can heat a region comparable to their own volume while they may chemically metasomatize a much greater region of normal mantle with their exotic constituents. Beneath Jericho, they could not have produced a laterally extensive heated region, say between 160 and 190 km depth. The heat-balance analysis with the light green triangle in Figure 12 and equation (11a) apply with the intruded kimberlites being the heat source. The effective excess heat of the metasomatizing kimberlites (including latent heat) is equivalent to an excess temperature of ~500 K. The observed temperature anomaly requires an equivalent layer of ~12.5 km thickness. This massive amount of intrusion is highly unlikely given that kimberlites are a low $\ll$1% partial melt of the bulk mantle. For example, a regional emplacement of 0.1% kimberlites would increase the regional temperature by only 0.5 K.

[35] Heat diffusion quickly returns a local region of increased temperature to its regional value. Mathematically, I use the temperature around an initially tabular region with a thickness X and an effective excess temperature ΔT_0 to represent an individual dike or a stockwork of dikes. The excess temperature is then

$$\Delta T = \frac{\Delta T_0 X}{\sqrt{4\pi\kappa t}} \exp\left[-\frac{x^2}{4\kappa t}\right], \qquad (12)$$

where $\kappa \equiv k/\rho C$ is thermal diffusivity and x is the distance from the center of the body (equation 4–163 of *Turcotte and Schubert* [1982]). The full width of the anomaly is $\sim 4\sqrt{\kappa t}$. For $\kappa = 0.75 \times 10^{-6}$ $m^2 s^{-1}$, the width is 19 km after 1 m.y. and 61 km after 10 m.y. For example, the excess temperature at the center of a 100-m wide stockwork would be 0.5% and 0.2%, respectively, of its initial value.

[36] Conversely, the volume of the Jericho kimberlite is large enough that its deep stockwork could have had brief local thermal effects in the mantle. Using its 200-km depth extent, a 1-m dike width, and an along-strike length of 14 km [*Cockenboo*, 1999] yields a volume of 3 km^3. An intruded volume of several cubic kilometers between 160 and 190-km depth is reasonable.

[37] Thus my preferred explanation for these data (Figure 12) is that the metasomatism and the elevated temperatures of the sheared xenoliths are a local feature associated with a kimberlite stockwork between ~160 and ~190 km depth, following the work of *Moore and Lock* [2001] on South African xenoliths. This nicely explains the large P-T scatter in the sheared xenolith data provided the erupting dike ascended from ~190-km depth. The scatter is signal telling about a highly variable temperature field on the scale of 10s of meters within the stockwork. The deep coarse xenolith and the pyroxenite points on the conductive geotherm represent regions outside the local stockwork that were not thermally affected by it or had cooled back to the ambient temperature. The metasomatized points lie to the right of the conductive geotherm. Metasomatizing magmas move upward and cannot increase the local temperature above the liquid adiabat from their source regions. The elevated temperature and the metasomatism of the deep sheared Jericho xenoliths do not represent regional features of the mantle in this hypothesis. My preferred regional geotherm is the lower left envelope of the array of points, the thick green line in Figure 12. I continue with the mechanics of stockwork formation in section 4.4.

3.2. Lesotho, Southern Africa

[38] Numerous kimberlites exist in Southern Africa. I discuss data from Lesotho to illustrate the geotherm sampled by kimberlites sourced by hot plume material (Figure 13). The samples come from Koa, Letsang, Monastery, Thaba Putsoa, Matsuku, Liquobong, and Lemphane [*Nixon*, 1973]. The eruption ages are ~90 Ma [*Allsopp and Barrett*, 1975; *Kramers and Smith*, 1983; *Davis*, 1977]. This date is based on a variety of methods and is grossly reliable, even though some kimberlite K-Ar and Ar-Ar ages are unreliable because of excess Ar [*Kelley and Wartho*, 2000].

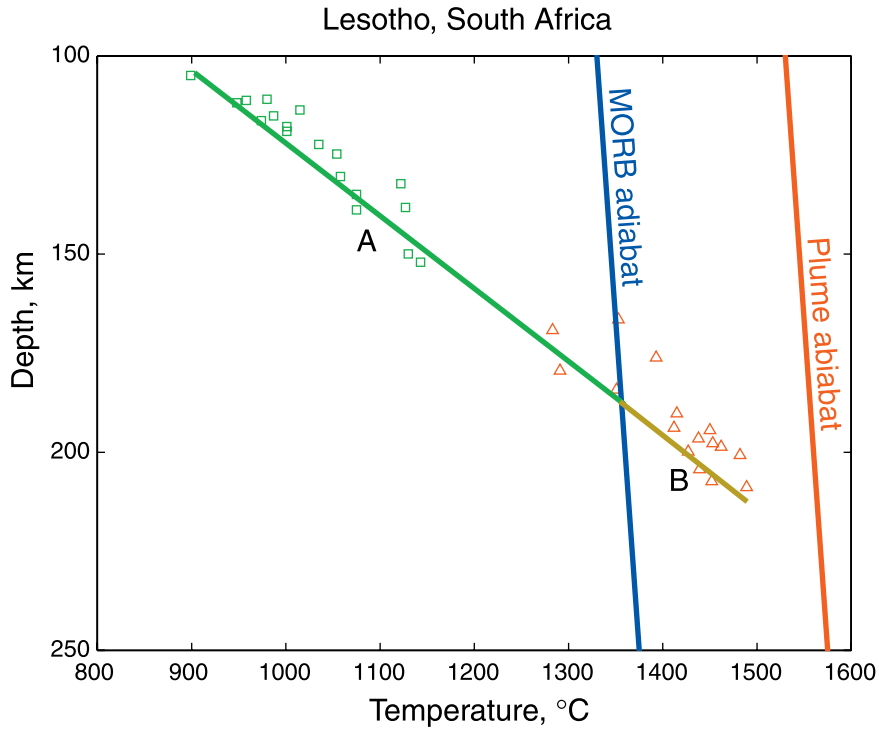

Figure 13. Xenolith depth and temperature from various kimberlites in Lesotho using the *Brey and Köhler* [1990] method (data provided by Cin-Ty Lee, 2002) plotted as in Figure 13. The shallow point group A constrains the shallow conductive geotherm. The deep point group B is hotter than the MORB adiabat and probably samples plume material.

[39] The observed composite geotherm consists of an upper linear part (line and points A) and a deeper part above the MORB adiabat along its extrapolation (line and points B). This geotherm resembles the model geotherm at 250-km distance at 2 m.y (Figure 4), that is, the geotherm through the top of a broad region of plume material, a common situation in Figure 3. There are no xenoliths from the deeper part of the geotherm beneath the plume material. This is not surprising in that one naively expects that the hottest material would have the highest fraction of melt and thus be the most likely source region.

[40] The presence of a plume in this region at ~90 Ma is likely but poorly constrained. The 183-Ma Karoo starting plume head produced flood basalts and dikes [*Duncan et al.*, 1997]. Its material probably cooled to the mantle adiabat in the ~90 m.y. between the Karoo and the Lesotho events (Figures 10 and 11). *Le Roex* [1986] and *Phillips et al.* [1998] suggest several possible plume tail tracks in the region. Overall, even the Karoo plume cannot be reliably traced to a modern hotspot and the number and location of active plumes is the South Atlantic is poorly constrained [*Sleep*, 2002]. In addition, plume conduits advect in the mantle and do not constitute a fixed array of points [e.g., *Steinberger*, 2002]. I do not attempt here to untangle the plume tracks in this region.

4. Sheared Xenoliths and Stresses

[41] As noted in section 3, deeper xenoliths often have sheared textures and shallow xenoliths coarse textures. It is tempting to use the temperature range defined by the sheared xenoliths to define the temperature range within the rheological boundary layer at the base of the lithosphere [*Sleep*, 2003]. I show that this inference is useful, but more complicated than it first appears in section 4.4. In the process, I quantify the tendency for kimberlites to form deep stockworks discussed in section 3.1.

[42] In section 4.1, I discuss membrane stresses and the shear stress associated with drag on the

base of the plate. In section 4.2, I show that the stresses associated with convection are important around downwellings. Petrologists infer the strain rate and stress magnitude within xenoliths before their time of extraction by studying the fabric [e.g., *Kennedy et al.*, 2002]. I discuss the implications of such data in section 4.3.

[43] I attempt to constrain the orientation and magnitude of stresses in the lithosphere. To do this, I need to consider nonlinear rheology explicitly, especially since petrologists assume such a rheology to obtain stress from xenoliths. Then the strain rate tensor is given by

$$\varepsilon'_{ij} = \frac{\tau_{ij}}{2\eta}\left[\frac{\tau}{\tau_{\mathrm{ref}}}\right]^{n-1}, \tag{13a}$$

η is a material property with dimensions of viscosity given by equation (3), $\tau \equiv \sqrt{\tau_{ij}\tau_{ij}}$ is the second invariant of the deviatoric stress tensor, and τ_{ref} is a reference stress. (One recovers linear rheology for $n = 1$.) The predictable regional parts of the stress tensor arise from membrane stresses in the plates, the stress traction on the base of the plate, and from secondary convection. It is useful to invert equation (13a) because kinematics constrains the membrane strain in the plate and the simple shear strain from plate drag. Then equation (13a) becomes

$$\tau_{ij} = \varepsilon'_{ij}[2\eta]^{1/n}\left[\frac{\varepsilon'}{\tau_{\mathrm{ref}}}\right]^{\left[\frac{1-n}{n}\right]}, \tag{13b}$$

where $\varepsilon' \equiv \sqrt{\varepsilon'_{ij}\varepsilon'_{ij}}$ is the second invariant of the strain rate tensor. I consider membrane stress and shear traction together because they are in balance over the area of a plate. I use dimensional arguments and simple calculations rather than attempting to consider any one region in detail.

4.1. Plate-Wide Force Balance

[44] The driving forces that move plates are balanced by the drag at the base of the plate. My purpose is to show that the horizontal membrane stresses associated with driving forces dominate at shallow depths and the shear stress on horizontal planes dominates at greater depths. A one-dimensional cross-section through the plate suffices because plates are much wider than thick. It includes the effect of temperature on viscosity within the lithosphere and initially ignores the perturbing effects of kimberlite dikes on stress.

[45] I follow *Zoback and Townend* [2001] to obtain the depth variation of membrane stress and shear traction. I consider strain rates for which kinematic constraints exist. The horizontal strain rate ε'_{yy}, where y is the direction of greatest horizontal tension (crudely that of plate motion), is constant with depth. (Continuity in two-dimensions requires that $\varepsilon'_{zz} = -\varepsilon'_{yy}$.) The horizontal extensional strain rate in stable (low-heat flow) cratons is $\sim 10^{-20}$ s^{-1}, while the strain rate in other midplate regions is less than $\sim 10^{-17}$ s^{-1} [*Zoback and Townend*, 2001]. The strain rate from plate drag is $\sim 10^{-14}$ s^{-1} in a 100-km thick shear zone beneath a plate moving at 30 mm yr^{-1}. I show by considering force balances that membrane stress and strain rate dominate at shallow depths while shear traction and shear strain rate dominate near the base of the lithosphere.

[46] Continuing to follow *Zoback and Townend* [2001], I obtain the distribution of horizontal stresses within the lithosphere. A shallow zone of frictional failure overlies a deeper zone of ductile creep, which is of most concern here. I assume for now that the shear traction is small enough that it can be ignored. The constant strain rate within the ductile regions is derived dimensionally from equation (13a)

$$\varepsilon'_{yy} = \frac{\tau_{yy}^{n}}{\tau_{\mathrm{ref}}^{n-1}\eta_0}\exp\left[\frac{-T_L(Z_L - z)}{T_\eta Z_L}\right], \tag{14}$$

where z is depth, the geotherm is linear, and the (horizontal) membrane stress τ_{yy}. The membrane stress varies with depth as

$$\tau_{yy} = \left[\varepsilon'_{yy}\eta_0\tau_{\mathrm{ref}}^{n-1}\right]^{1/n}\exp\left[\frac{T_L(Z_L - z)}{nT_\eta Z_L}\right]. \tag{15}$$

The horizontal force per length of plate is the integral with depth of the membrane stress in equation (15)

$$F = \int_0^{Z_1}\frac{\tau_1 s}{Z_1}ds + \int_{Z_1}^{\infty}\tau_{yy}ds = \left[\varepsilon'_{yy}\eta_0\tau_{\mathrm{ref}}^{n-1}\right]^{1/n} \cdot \exp\left[\frac{T_L(Z_1 - z)}{nT_\eta Z_L}\right]\left[\frac{Z_1}{2} + \left[\frac{nZ_L T_\eta}{T_L}\right]\right], \tag{16}$$

where the limit Z_1 represents the top of the ductile zone and s is a dummy variable for depth. The first

term on the left-hand side represents linear increase of frictional stress in the brittle lid above Z_1. (It could be modified to include a more complicated crust.) The second term on the left-hand side represents ductile creep. The product of the first two terms on the right-hand side of equation (16) is the stress τ_1 at depth Z_1. The two terms in the final bracket represent friction and ductile creep. The latter term in this bracket is the depth range R for the temperature to vary by nT_η. Equation (16) then becomes

$$F = \tau_1 \left[\frac{Z_1}{2} + R \right] \tag{17}$$

[47] I obtain the horizontal shear traction τ_{yz} from plate drag by considering the force balance in the plate. I first perform a local mass balance in the column within a craton where there are no local lateral variations in density. The derivative of $\partial F/\partial y$ is equal to the shear traction τ_{yz}. Extending this balance over the entire width of the plate Y, the shear traction is dimensionally

$$\tau_{yz} = F/Y. \tag{18}$$

In the upper region of the plate where membrane stresses dominate, this implies that the ratio of shear traction to membrane stress (and the ratio of shear strain rate to membrane strain rate) increases with depth as

$$\frac{\tau_{yz}}{\tau_{yy}} = \left[\frac{R + Z_1/2}{Y} \right] \exp \left[\frac{-T_L(Z_1 - z)}{nT_\eta Z_L} \right]. \tag{19}$$

The ratio is small $\sim$0.01 at the depth Z_1 because the aspect ratio of the depth term $R + Z_1/2$ (tens of km) to the plate width (thousandss of km) is $\sim$100.

[48] The ratio increases downward, eventually reaching a point where the membrane stress and the shear traction are comparable. Both terms enter into the invariant in equation (13a). Below this transition, the shear strain dominates the invariant in equations (13b) and (15) does not apply.

[49] The observed thickness of the rheological boundary layer in equation (5) constrains the length scale $nT_\eta Z_L/T_L$ of the increase of the ratio in equation (19). That is, the rheological layer thickness cannot be >300 km without producing obvious curvature at the base of the xenolith pressure-temperature array. Letting T_L be 1300 K and Z_L be 200 km constrains the length scale to be less than 19 km for a linear rheology and less than 32 km for . In the two cases, the ratio in equation (19) varies by factors of 107 and 2700, respectively, between the moho at say 35 km depth and the top of the rheological boundary layer at say 185 km depth.

[50] From this I conclude that the shear traction and shear strain rate dominate over the membrane stress and the membrane strain rate within the rheological boundary layer and the deepest lithosphere as shown on Figure 14. The result is applicable to the ascent of kimberlites, as dikes intrude perpendicular to the greatest tensile stress. Thus shallow dikes intrude in the xz-plane perpendicular to the direction of plate motions. Deeper dikes within the zone where the shear traction dominates intrude within 45° dipping planes striking in the x-direction perpendicular to plate motions. Dikes curve from one orientation to the other in the transition zone where both components of the stress tensor are comparable. In the Earth, the local direction of maximum lithospheric tension need not line up with the direction of plate motion. The strike as well as the dip of the dike then changes within the transition zone.

4.2. Effect of Convection on Dike Intrusion

[51] Pronounced lateral density contrasts exist at the top of downwellings and produce strong stress concentrations within the thermal boundary layer (Figure 15). In a nonlinear fluid, these stress concentrations greatly increase the strain rate, leading to avalanches [*Reese et al*, 1998, 1999]. The density contrasts at the top of downwellings scale with the temperature range across the rheological boundary ΔT_{rheo} in equation (5). The thickness of the rheologically active boundary layer is dimensionally

$$\Delta Z_{\text{rheo}} = \frac{\Delta T_{\text{rheo}} Z_L}{T_L}. \tag{20}$$

Stress concentrations exist in and around downwellings and their extent scales with the rheologi-

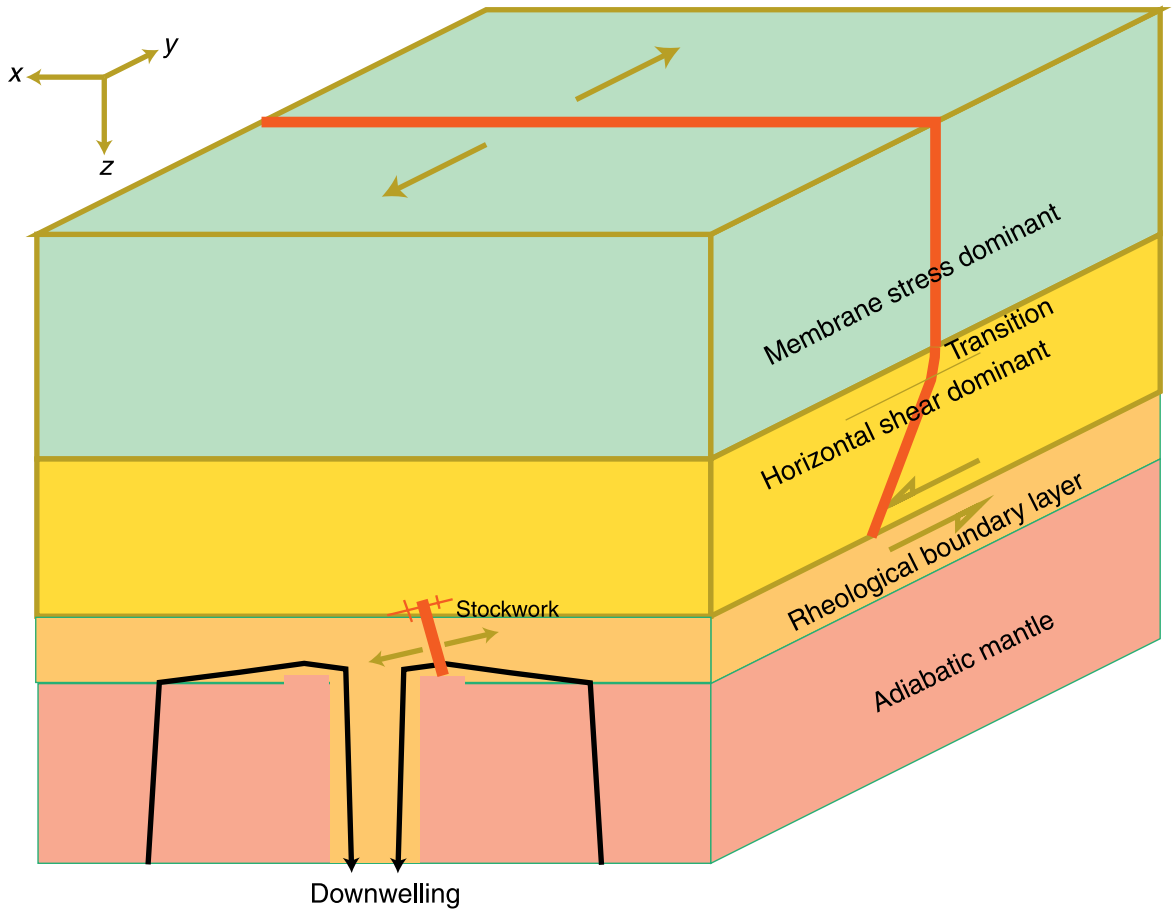

Figure 14. Schematic diagram of stresses and dike directions within the lithosphere. From bottom up, convection cells align in the direction of plate motion within the adiabatic mantle and the rheological boundary layer. Stress concentrations occur around downwellings. Dikes ascend from the flanks of downwellings and form stockworks near the top of the regional boundary layer. Horizontal shear traction dominates the stress tensor between the rheological boundary layer and the strong upper part of the lithosphere. Dikes traversing this region dip at ~45°. Membrane stress dominates in the strong upper part of the lithosphere causing vertical dikes. The plane of dikes curves between 45° and vertical in the transition region between the upper and lower part of the lithosphere where membrane stress and shear traction are comparable.

cal thickness ΔZ_{rheo}. The stresses associated with convection are dimensionally

$$\tau_v = \frac{\rho g \alpha \Delta T_{\text{rheo}}^2 Z_L}{T_L} \tag{21}$$

For the parameters in the models (including $\Delta T_{\text{rheo}} = 144$ K), the convective stress is 3.2 MPa, in general agreement with ~1 MPa in Figure 15. The stress concentrations extend upward into rigid lithosphere, which supports the underlying density contrasts. The dimensions of these features scale with the spacing between downwellings.

[52] This is significant, as plate-wide force balance considerations limit the shear traction beneath cratons to a few MPa [*Sleep*, 2003]. The inference that convection supplies the observed mantle heat flow to cratons also constrains the shear traction as the viscosity at given heat flow scales as T_η^4 in equation (4). In the models, the viscosity is 0.657×10^{19} Pa s, implying a shear traction of 0.657 MPa at a strain rate of 10^{-14} s^{-1}. That is, the shear traction and the convective stresses are comparable.

[53] This inference and the inferences in section 4.1 yield a qualitative sequence of events leading sometimes to the intrusion of a kimberlite to the

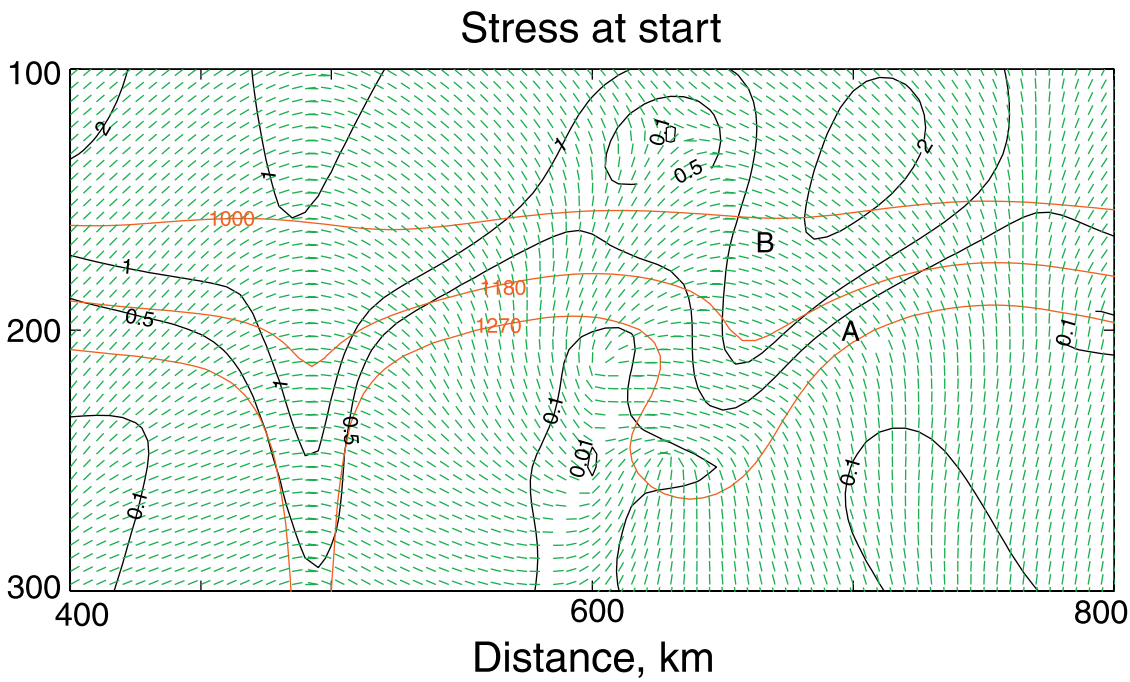

Figure 15. Dikes intrude parallel compressive stress directions (green) in the starting model in Figure 1. The second invariant $\sqrt{\tau_{ij}\tau_{ij}}$ is contoured as the maximum resolved shear stress in two dimensions (black). Isotherms are contoured in red. A strong downwelling exists at 500-km distance and the flanks of a nascent downwelling are at 700-km distance. See text.

surface (Figure 14). Convection cells tend to strike in the direction of the shear traction from plate motions [*Richter*, 1973]. Stresses favorable for extrusion of melt exist at the upwellings on the immediate flanks of active and nascent downwellings. The stresses from convection and the shear traction interact to produce dikes with a nonvertical dip. The dikes open to a width of

$$X = \frac{L\Delta P}{E}, \tag{22}$$

where L is the length (that is the shortest in-plane dimension) of the dike, ΔP is the excess pressure of the dike relative to the more tensile prinicipal stress, and E is the elastic (Young's) modulus (about 2×10^{10} Pa in the upper mantle). Conversely, ΔP is the stress change produced by a dike of a given width. The stress associated with convection limits the width to which dikes open above downwellings. For example, the 1 MPa stress can open 10-km long dikes by 0.5 m.

[54] The dike trajectories sometimes carry them into regions of low deviatoric stress and regions where the dikes are horizontal. Both effects tend to cause the dikes to stagnate. For example, I consider the flank of the nascent upwelling at 700-km distance and 200-km depth in Figure 15 (point A). Higher stresses extend downward into the boundary layer. Dikes once started there intruded up and to the left becoming horizontal around 650-km distance and 180-km depth (point B).

[55] I now consider the effect of gravity and the lower density of the dike than the mantle on stresses. The pressure change from gravity in the dike relative to lithostatic pressure is

$$\Delta P_g = \Delta\rho g H, \tag{23}$$

where $\Delta\rho$ is the density deficit of the dike relative to the mantle and H is the vertical extent of the dike. For example, the pressure changes by 39 MPa over a 10-km depth interval for a 400 kg m^{-3} density deficit. That is, the fluid pressures associated with gravity are likely to dominate over the convective stresses once dikes have a significant vertical extent. The deviatoric stress then still controls the orientation of the dikes.

[56] The interaction of the stresses associated with convection with gravitationally produced fluid pressures within dikes leads to the formation of stockworks if the magma ascends in batches [*Parsons et al.*, 1992]. The initial dike ascends in a plane perpendicular to the more tensile stress. It fills and freezes, reducing the tension parallel to the dike. This stress relaxation may be enough that the stress perpendicular to the frozen dike is no longer the most tensile stress. Subsequent dikes intrude perpendicular to the new most tensile stress forming a stockwork. In an elastic medium, enough frozen dikes can raise all the principal stresses to the fluid pressure, precluding any further intrusion.

[57] This situation is only temporary in the rheological boundary layer where the host material can accommodate some amount of ductile deformation. Ductile creep relaxes the stresses associated with the stockwork and more dikes may thus continually intrude. That is, a large stockwork can build up only where the host material can deform ductily to some extent. Overall, a region with low stresses, like parts of the top of the rheological boundary layer, is likely to have its principal stresses changed and to be a region where dikes form a stockwork.

[58] Once the kimberlite magma succeeds in intruding well above the top of the rheological boundary layer, its path is easier. Initially it intrudes as a dipping dike. It then becomes a vertical dike perpendicular to the membrane tension, which increases upward.

4.3. Comparison With Observed Xenolith Stresses

[59] I discuss the suite of xenoliths studied by *Kennedy et al.* [2002] from the Jericho pipe in Canada to continue with the real example from section 3.1. They inferred the strain rate and stress magnitude from their samples. They did not attempt to determine the orientation of the stress tensor, a very difficult project with xenoliths. Their samples fall into two groups.

[60] The first group consists mainly of shallow coarse samples but includes some deep and some sheared samples. The stress magnitude decreases slowly from 7 MPa at 70-km depth to 3 MPa at 190-km depth. The strain rate increases from $\sim 10^{-19}$ to 10^{-10} s^{-1}.

[61] The nearly constant stress level with depth is expected if the horizontal shear traction from plate drag is the dominant effect below ~70 km depth. The data are compatible with this inference. The strain rates are all faster than the expected extensional strain rate of 10^{-20} s^{-1} for stable cratons [*Zoback and Townend*, 2001], which implies that the stresses are lower than those in the overlying strong region of the lithosphere. However, the deep strain rate is orders of magnitude higher than the expected strain rate from plate drag, 10^{-14} s^{-1}. It is also grossly too high for convection at the base of the plate as well as driving drag at the base of the plate, as these rates scale crudely to those for plate motion. (Physically, the viscous dissipation, $\varepsilon'_{ij}\tau_{ij}$, is limited by the amount of gravitational work done by the convection.) It is conceivable that the high value of computed deep strain rate results from imprecision of the method.

[62] This inference of dominance of shear traction over membrane stress, however, gives rise to a testable prediction that might conflict with the general inference that cratonal xenolith provinces correlate with surface geological provinces [e.g., *Pearson*, 1999]. (Petrologists traditionally draw vertical dikes in the mantle in their schematic diagrams.) In the case of Jericho, the deeper xenoliths would be offset horizontally from the surface pipe by ~120 km by a 45° dipping dike between 70 and 190 km depth. (The predicted 45° dip of dikes deep in the lithosphere is testable should a kimberlite deign to ascend near seismic stations.)

[63] The second group of data consists of samples having ~100-MPa stresses and $\sim 10^{-5}$ s^{-1} strain rates. I attribute these points to the local effects of dike intrusion in a stockwork. The stresses and strain rates are too large to be sustained even for a year as viscous dissipation would increase the temperature by several 1000 K. More likely the stresses and strain rates represent a local transient event. *Kennedy et al.* [2002] point out the local feature of bimodal size distribution where differ-

ent parts of individual xenoliths belong to each group. The dikes extending over the depth range of the high-stress xenoliths, ~30 km, can locally generate 100 MPa, especially near crack tips and other irregularities. The megacrystalline xenoliths, the metasomatism, and some elevated temperatures indicate that the deep xenoliths came from an active stockwork as discussed in scetion 3.1.

4.4. Relationship of Sheared Xenoliths to Rheological Boundary Layer Temperature Range

[64] The most sheared Jericho xenoliths appear to represent a local event. They are thus not direct evidence of the thickness of (and the temperature range across) the rheological boundary layer. The curvature of the lower envelope of the xenolith pressure-temperature array from single eruptions is a more reliable indicator of the rheological temperature range. The temperature range of sheared xenoliths, however, is an indirect constraint on the rheological temperature range though the dynamic processes that form kimberlite stockworks.

[65] In section 4.2, I noted dikes may stagnate within and just above the rheological boundary layer. Ductile flow near stress concentrations associated with dikes can occur at a significant rate in this region, unlike the more rigid lithosphere above it. This allows the stresses to relax to their pre-dike values, form a high-stress fabric, and lets more dikes intrude to build up the stockwork. This implies that sheared xenoliths can form somewhat above the rheological boundary layer and that the temperature range of sheared xenoliths is an upper limit on the rheological temperature range. In support of this hypothesis, Os isotopic studies indicate that some sheared xenoliths from the Kaapvaal craton are ancient parts of the lithosphere, not transient material in a convecting boundary layer [*Pearson*, 1999].

5. Geological Implications and Conclusions

[66] The pressure-temperature arrays of cratonic xenoliths constrain the processes that form kimberlites as well as the nature of convection beneath cratons. Most reliably, the conductive part of the array gives the heat flow at the time of the eruption. The curvature (or lack thereof) at the base of the array constrains the temperature range across the rheological boundary layer.

[67] Other inferences are more difficult. In principle, one should be able to determine the lateral variability of the geotherm along the strike (and dip) of a kimberlite dike by the scatter in the observed array. In the data that I examined, local heating associated with metasomatism by the kimberlite magma is a more profound source of scatter. The low-temperature envelope of a depth-temperature array (thick green line, Figure 12) is the preferred estimate of the geotherm because metasomatism by hot magmas can only raise the temperature.

[68] One effect of plumes is to thin the lithosphere and increase the geothermal gradient throughout the lithosphere. The eventual thinning is modest. For example, a 40-km thick layer of plume material thins the lithosphere by 12 km. Still *Bell et al.* [2003] observe the effect in Southern Africa where there have been multiple plume events. A portion of the xenolith array is hotter than the MORB adiabat beneath Lesotho, indicating the presence of plume material. Computations indicate that material remains hotter than the MORB adiabat for less than 20 m.y. after it has ponded beneath the base of a flat lithosphere.

[69] A qualitative difference between plume-affected lithosphere and normal lithosphere results because plume material ponds beneath local regions of thin lithosphere [e.g., *Sleep et al.*, 2003]. This heats up the regions of thin lithosphere relative to the thicker cratons. For example, the process may have heated the lithosphere in mobile belts in Southern Africa out of the diamond stability field. Otherwise, the lithosphere tends to (gradually and everywhere) approach the thickness that is in equilibrium with the heat flow from the underlying convection. I concur with *Bell et al.* [2003] that the features observed in xenolith arrays are in part transient.

[70] The interaction of the stresses associated with convection, the shear traction associated with drag at the base of the plate, and the membrane stress in the plate complicates dike ascent. The stress concentrations near downwellings start dikes. Regions of low deviatoric stress and horizontal dike planes are likely stagnate dikes within and just above the rheological boundary layer. These dikes are likely to form stockworks in this deformable region. Abundant megacrysts and recently heated and high-stress sheared xenoliths are plucked once the dikes ascend to the surface. The Jericho samples in Figure 12 may represent this situation.

[71] In contrast, kimberlites fed by plume material start well below the normal top of the rheological boundary layer. The shear traction from plate drag is quite low because the low viscosity plume material lubricates plate motion. Dikes have considerable excess pressure once they arrive at the normal temperature of the rheological boundary layer and tend to continue upward to the surface. There is much less opportunity to form stockworks. The quickly plucked xenoliths represent the actual geotherm with less scatter. The Lesotho samples may represent numerous such events over a geologically brief period of time.

[72] Ideally, the methods for determining the pressure-temperature array, the stress magnitude, and the MORB adiabat should be self-consistent. More importantly, the methods used for determining stress magnitude should be self-consistent with the rheology in the convection models and the long-term thermal state of the lithosphere. There is considerable need for improvement as even the low-stress samples discussed in section 4.3 yield unreasonable strain rates for any widespread long-lived process. Once this is done, it should be possible to quantitatively model the ascent of dikes and the formation of stockworks in three dimensions.

Acknowledgments

[73] This research was in part supported by NSF grant EAR-0000747. I thank David Bell for a preprint of his paper. I thank Cin-Ty Lee for the compilation of xenolith pressures and temperatures and Joe Boyd for help in finding sample localities. I thank Andy Nyblade for reading the paper and Louis Moresi, Roberta Rudnick, and J.K. Russell for helpful reviews.

References

Allsopp, H. L., and D. R. Barrett, Rb-Sr age determination on South African Kimberlite pipes, *Phys. Chem. Earth*, *9*, 605–617, 1975.

Anderson, O. L., The role of fracture dynamics in kimberlite pipe formation, in *Kimberlites, Diatremes, and Diamonds; Their Geology, Petrology, and Geochemistry*, edited by F. R. Boyd and H. O. A. Meyer, pp. 344–353, AGU, Washington, DC, 1979.

Andrews, D. J., Numerical simulation of sea floor spreading, *J. Geophys. Res.*, *77*, 6470–6481, 1972.

Bell, D. R., M. D. Schmitz, and P. E. Janney, Mesozoic thermal evolution of the southern African mantle lithosphere, *Lithos*, in press, 2003.

Brey, G. P., and T. Köhler, Geothermobarometry in four-phase lherolites: II. New thermobarometers and practical assessment of existing thermobarameters, *J. Petrol.*, *31*, 1353–1378, 1990.

Cockenboo, H. O., History and process of emplacement of the Jericho (JD-1) kimberlite pipe, northern Canada, in *The Dawson Volume, Proceedings of the VIIth International Kimberlite Conference*, edited by J. J. Gurney et al., pp. 125–133, Red Roof Design, Cape Town, South Africa, 1999.

Davaille, A., and C. Jaupart, Thermal convection in lava lakes, *Geophys. Res. Lett.*, *20*, 1827–1830, 1993a.

Davaille, A., and C. Jaupart, Transient high-Rayleigh-number thermal convection with large viscosity variations, *J. Fluid Mech.*, *253*, 141–166, 1993b.

Davaille, A., and C. Jaupart, The onset of thermal convection in fluids with temperature-dependent viscosity: Application to the oceanic mantle, *J. Geophys. Res.*, *99*, 19,853–19,866, 1994.

Davis, G. L., The ages and uranium contents of zircons from kimberlites and associated rocks, *Carnegie Inst. Washington Year Book*, *76*, 631–635, 1977.

Doin, M.-P., L. Fleitout, and U. Christensen, Mantle convection and stability of depleted and undepleted continental lithosphere, *J. Geophys. Res.*, *102*, 2771–2787, 1997.

Duncan, R. A., P. R. Hopper, J. Rehacek, J. S. Marsh, and A. R. Duncan, The timing and duration of the Karoo igneous event, southern Gondwana, *J. Geophys. Res.*, *102*, 18,127–18,138, 1997.

Heaman, L. M., and B. A. Kjargaard, Timing of eastern North American kimberlite magmatism: Continental extension of the Great Meteor hotspot track, *Earth Planet. Sci. Lett.*, *178*, 253–268, 2000.

Kelley, S. P., and J. A. Wartho, Rapid kimberlite ascent and the significance of Ar-Ar ages in xenolith phlogopites, *Science*, *289*, 609–611, 2000.

Kennedy, L. A., J. K. Russell, and M. G. Kopylova, Mantle shear zones revisited: The connection between the cratons and mantle dynamics, *Geology*, *30*, 419–422, 2002.

Kopylova, M. G., J. K. Russell, and H. O. Cockenboo, Mapping the lithosphere beneath the north central Slave Craton, in *The Dawson Volume, Proceedings of the VIIth International Kimberlite Conference*, edited by J. J. Gurney et al., pp. 468–479, Red Roof Design, Cape Town, South Africa, 1999a.

Kopylova, M. G., J. K. Russell, and H. Cookenboo, Petrolgy of peridotite and pyroxenite xenoliths from the Jericho kimberlite: Implications for the thermal state of the mantle beneath the Slave craton: Northern Canada, *J. Petrology*, *40*, 79–104, 1999b.

Kramers, J. D., and C. B. Smith, A feability study of U-Pb and Pb-Pb dating of kimberlites using groundmass mineral fractions and whole-rock samples, *Chem. Geol*, *41*, 23–38, 1983.

Le Roex, A. P., Geochemical correlation between southern African kimberlites and South Atlantic hotspots, *Nature*, *324*, 243–245, 1986.

Moore, A. E., and N. P. Lock, The origin of mantle-derived magacrysts and sheared peridotite from kimberlites in the northern Lesotho Orange Free State (South Africa) and Botswana pipe clusters, *S. Afr. J. Geol.*, *104*, 23–38, 2001.

Moore, W. B., G. Schubert, and P. Tackley, Three-dimensional simulations of plume-lithosphere interaction at the Hawaiian swell, *Science*, *279*, 1008–1011, 1999.

Nixon, P. H., (Ed.), *Lesotho Kimberlites*, Lesotho Natl. Dev. Corp., Maseru, Lesotho, 1973.

O'Neill, C., L. Moresi, A. Lenardic, and K. Cooper, Inferences on Australia's heat flow and thermal structure from mantle convection models, *Spec. Publ. Geol. Soc. Aust.*, *22*, 163–178, 2003.

Parsons, T., N. H. Sleep, and G. T. Thompson, Host rock rheology on the emplacement of tabular intrusions: Implications for underplating of extending crust, *Tectonics*, *11*, 1348–1356, 1992.

Pearson, D. G., The age of continental roots, *Lithos*, *48*, 171–194, 1999.

Phillips, D., K. J. Machin, G. B. Kiviets, L. F. Fourie, M. A. Roberts, and E. M. W. Skinner, A petrographic and Ar-40/Ar-39 geochronoloical study of the Voorspoed kimberlite, South Africa: Implications for the origin of Group II kimberlites, *S. Afr. J. Geol.*, *101*, 299–306, 1998.

Price, S. E., J. K. Russell, and M. G. Kopylova, Primitive magma from the Jericho pipe, NWT, Canada: Constraints on primary melt chemistry, *J. Petrol.*, *41*, 789–808, 2000.

Reese, C. C., V. S. Solomatov, and L.-N. Moresi, Heat transport efficiency for stagnant lid convection with dislocation viscosity: Application to Mars and Venus, *J. Geophys. Res.*, *103*, 13,643–13,657, 1998.

Reese, C. C., V. S. Solomatov, and L.-N. Moresi, Non-Newtonian stagnant lid convection and magmatic resurfacing on Venus, *Icarus*, *139*, 67–80, 1999.

Richter, F. M., Convection and the large-scale circulation of the mantle, *J. Geophys. Res.*, *78*, 8735–8745, 1973.

Rudnick, R. L., and A. A. Nyblade, The thickness and heat production of Archean lithosphere: Constraints from xenolith thermobarometry and surface heat flow, in *Mantle Petrology: Field Observations and High Pressure Experimentation: A Tribute to Francis R. (Joe) Boyd*, edited by Y. Fei, C. M. Bertka, and B. O. Mysen, *Spec. Publ. Geochem. Soc.*, *6*, 3–12, 1999.

Saal, A. E., E. H. Hauri, C. H. Langmuir, and M. R. Perfitt, Vapour undersaturation in primitive mid-ocean-ridge basalt and the volatile content of the Earth's upper mantle, *Nature*, *419*, 451–455, 2002.

Sleep, N. H., Ridge-crossing mantle plumes and gaps in tracks, *Geochem. Geophys. Geosyst.*, *3*(12), 8505, doi:10.1029/2001GC000290, 2002.

Sleep, N. H., Survival of Archean cratonal lithosphere, *J. Geophys. Res.*, *108*(B6), 2302, doi:10.1029/2001JB000169, 2003.

Sleep, N. H., C. J. Ebinger, and J.-M. Kendall, Defection of mantle plume material by cratonic keels, in *The Early Earth: Physical, Chemical and Biological Development*, edited by C. M. R. Fowler, *Spec. Pub. Geol. Soc.*, *199*, 135–150, 2003.

Solomatov, V. S., Scaling of temperature- and stress-dependent viscosity convection, *Phys. Fluids*, *7*, 266–274, 1995.

Solomatov, V. S., and L.-N. Moresi, Scaling of time-dependent stagnant lid convection: Application to small-scale convection on Earth and other terrestrial planets, *J. Geophys. Res.*, *105*, 21,795–21,817, 2000.

Spera, F. J., Carbon-dioxide in petrogenesis: 3. Role of volatiles in the ascent of alkaline magma with special reference to xenolith-bearing mafic lavas, *Contrib. Mineral. Petrol.*, *88*, 217–232, 1984.

Steinberger, B., Motion of the Easter hot spot relative to Hawaii and Louisville hot spots, *Geochem. Geophys. Geosyst.*, *3*(11), 8503, doi:10.1029/2002GC000334, 2002.

Turcotte, D. L., and G. Schubert, *Mantle Geodynamics Applications of Continuum Pysics to Geological Problems*, 450 pp., John Wiley, Hoboken, N. J., 1982.

Zoback, M. D., and J. Townend, Implications of hydrostatic pore pressures and high crustal strength for the deformation of intraplate lithosphere, *Tectonophysics*, *336*, 19–30, 2001.